INTERNATIONAL JOURNAL FOR NUMERICAL METHODS IN FLUIDS
Int. J. Numer. Meth. Fluids 2018; **00**:1–24
Published online in Wiley Online Library (www.onlinelibrary.wiley.com). DOI: 10.1002/fld.4668

A localized artificial diffusivity method to simulate compressible multiphase flows using the stiffened gas equation of state

Mohamad Aslani and Jonathan D. Regele*

Department of Aerospace Engineering, Iowa State University, Ames, IA 50011

SUMMARY

The development of numerical approaches to perform direct numerical simulations of compressible multiphase flows has been an active field of research for several years. Proper treatment of fluid interfaces is crucial as important physics occur in this infinitesimally small region. Furthermore, the compressibility of the fluid requires proper treatment of discontinuities. Artificial diffusivity is among a number of methods widely used for compressible flows. The present study develops a general form of consistent artificial diffusion fluxes and extends the localized artificial diffusivity method for high-order central schemes to solve multiphase flows with an interface capturing method. These fluxes ensure an oscillation-free interface for pressure, velocity, and temperature without employing a sharpening technique. Moreover, high-order representation of all scales in the flow helps capture the wide range of instabilities inherent in these flows. The goal is to develop an approach capable of performing high fidelity simulations supported by physics-driven validation. This is achieved by solving the five-equation model with the stiffened gas equation of state using the proposed method for multicomponent and multiphase flows on a variety of one and two-dimensional problems.

Received . . .

KEY WORDS: Artificial diffusion flux, Compressible multi-phase flows, Interface capturing, Stiffened gas equation of state, Five-equation model

1. INTRODUCTION

Compressible multiphase flows are present in many engineering applications, such as supersonic combustion, erosion due to cavitation, and breakup of liquid jets at high speeds. Commonly prone to oscillations and numerical errors, discontinuities such as shock waves and material interfaces with high-density ratios can be challenging for numerical simulations. Moreover, high accuracy is required to capture the wide range of instabilities that may be present in these flow (e.g. Kelvin-Helmholtz to Richtmyer-Meshkov).

In the Eulerian framework, the simulation of compressible interfacial flows is typically divided into two major groups, namely interface tracking and capturing. Examples of tracking methods include all forms of level set [1, 2, 3], as well as front-tracking methods [4, 5, 6]. Although these methods have been used to study a wide range of problems [7, 8], they are geometrically complex and computationally expensive. Interface capturing methods, on the other hand, are relatively

*Correspondence to: jregele@lanl.gov, Department of Aerospace Engineering, Iowa State University, Ames, IA.

straightforward to implement and can handle complex topological changes. Moreover, they easily extend to multiple phases, higher dimensions, and higher orders of accuracy [9, 10].

In an interface capturing method, similar to shock capturing, the assumed sharp interface between the two fluids is relaxed across a number of grid points, converting it to an artificial mixture zone. However, this interface is prone to spurious oscillation errors. These errors occur due to different properties of fluids entering the equation of state (EOS) and violating the equilibrium condition at the interface and creating pressure, velocity or temperature oscillations. In the context of interface capturing methods, Abgrall [11] was the first to highlight and fix pressure and velocity oscillation errors in the interface of a gas-gas system with different thermophysical properties. Later, Shyue [12, 13, 14] extended the same approach to gas-liquid or gas-solid systems using Mie–Grüneisen and modified van der Walls EOS. Usually an extra (usually non-conservative) equation for specific heat ratios and fitting parameters in EOS or mass fractions are required to preserve equilibrium at the interface. A similar methodology was developed that uses an advection equation for the volume fraction to transport the properties of the stiffened gas EOS [15]. Alahyari and Johnsen [10] further extended the ability to calculate oscillation-free temperature profiles by using an isothermal interface. However, temperature is often ignored [9,16] when temperature-dependent phenomena like heat diffusion, reaction or phase change effects are negligible.

Another difficulty arising in interface capturing is the smearing of fluid interfaces. A variety of high-order methods [9, 16, 17], anti-diffusion techniques [18, 19] and interface sharpening methods [20, 21, 22, 23, 24] have been developed to resolve this problem. Caution is required when using interface sharpening techniques as nonphysical terms introduced into governing equations may facilitate mass, momentum and/or energy loss in the system. Moreover, these terms may not be compatible with the thermodynamic mixture model in the interface [22]. For example, authors in [20, 23] propose an algorithm to sharpen volume fractions and partial densities at a solution time-step and leave the rest of variables to see the sharpened profiles in the next time-step. This raises the question of consistency when using these techniques and recent work has been done to address some of these difficulties [25, 26].

Adding artificial diffusion is a classical method to capture discontinuities in compressible flows. More recently, in an extension to earlier work on hyperviscosity [27, 28] the idea of adding localized artificial transport-like diffusion terms to the physical equations is gaining more interest [29]. These methods are particularly interesting because of their simple formulation, straightforward implementation, low computational cost and most importantly high-accuracy. The latter is desirable for simulation of compressible flows with material discontinuities where the flow regime is prone to instabilities and turbulence. Moreover, Johnsen et al. [30] performed an extensive study on methods to solve compressible turbulent flows and concluded that high-order upwind-biased schemes (finite volume WENO, for instance) could be dissipative for the broad range of scales that might exist in a flow compared to central difference based methods, especially when considering viscous simulations where schemes like WENO are relatively expensive compared to central and Localized Artifical Diffusion (LAD) schemes (see the comparison of the methods in [30, 31, 32, 33]).

Simulation of multiphase flows introduces a unique type of material discontinuity in which the material density and thermophysical properties vary abruptly across the interface. Terashima et al. [34] introduced artificial diffusion terms specifically designed for the interface of a gas-gas system with different specific heat ratios. The assumption of pressure and velocity equilibrium between the two phases when they advect under constant pressure and velocity are central in all of the proposed methods. With these models in hand, a study of central schemes with localized artificial diffusivity, which takes into account multiphase systems (arbitrary number of gas and liquids), has yet to be proposed.

The objective of the current study is to develop accurate and consistent artificial (numerical) diffusion terms (fluxes) for compressible multiphase and multicomponent flows that do not produce oscillations in pressure and velocity in simulations of fluids with shocks and interfaces. An interface capturing approach is used to resolve the fluid interface across several grid points. While a stiffened EOS is used to close the system, the approach is general in that it applies to a wide class of artificial

diffusion methods for an arbitrary number of fluids, mass or volume fraction models, and different EOSs in which they all inherit the mechanical equilibrium condition of the current method.

This article is organized as follows. In Sec. 2, the physical model is described followed by a derivation of novel numerical diffusion fluxes in Sec. 3. In Sec. 4, the numerical method along with the derived artificial diffusion terms are briefly described and finally verified using a range of test problems in Sec. 5.

2. MATHEMATICAL MODEL

2.1. *Mass, momentum, and energy conservation laws*

The compressible Navier-Stokes equations govern each individual component or phase. Most of the usual closure models for interfacial variables result in equilibrium conditions at the interface for pressure and velocity. This condition reduces the number of equations, resulting in a model with a single unknown velocity and pressure for all components. If the volume fraction of fluid k ($\alpha^{(k)}$) is used to differentiate it from other components, conservation equations for mass, momentum and energy can be written in the following form (assuming no mass transfer, i.e. immiscible fluids),

$$\frac{\partial}{\partial t}(\rho^{(k)}\alpha^{(k)}) + \frac{\partial(\rho^{(k)}\alpha^{(k)}u_j)}{\partial x_j} = 0, \tag{1a}$$

$$\frac{\partial \rho u_i}{\partial t} + \frac{\partial}{\partial x_j}(\rho u_i u_j + p\delta_{ij}) = \frac{\partial \tau_{ij}}{\partial x_j} + f_i, \tag{1b}$$

$$\frac{\partial \rho e_t}{\partial t} + \frac{\partial}{\partial x_j}\left(u_j(\rho e_t + p)\right) = \frac{\partial}{\partial x_j}(u_i\tau_{ij} - Q_j) + u_j f_j, \tag{1c}$$

$$\frac{\partial \alpha^{(k)}}{\partial t} + u_j\frac{\partial \alpha^{(k)}}{\partial x_j} = 0, \tag{1d}$$

where $\rho^{(k)}\alpha^{(k)}$, p, and e_t are scalars representing the density of component k, pressure and total non-chemical energy (or briefly total energy). Velocity in the i^{th} direction is u_i and δ_{ij} is the identity tensor. The total density (ρ) is the summation of each individual component's density or $\rho = \sum_k \rho^{(k)}\alpha^{(k)}$ and the total energy is the summation of internal and kinetic energies: $e_t = e + u_j u_j/2$. The viscous stress tensor (τ_{ij}) and heat flux due to conduction (Q_j) are

$$\tau_{ij} = \mu\left(\frac{\partial u_i}{\partial x_j} + \frac{\partial u_j}{\partial x_i} - \frac{2}{3}\frac{\partial u_k}{\partial x_k}\delta_{ij}\right), \tag{2}$$

$$Q_j = -\kappa\frac{\partial T}{\partial x_j}, \tag{3}$$

where μ and κ are the dynamic shear viscosity and heat conductivity coefficient, respectively. Any force applied to the fluid volume is represented by f_j with the corresponding energy term $u_j f_j$.

For two-component flows, the above system is the well-known quasi-conservative five-equation model of Allaire et al. [15]. The non-conservative advection Eq. 1d for volume fraction has been widely used in the literature [35, 9, 15, 36, 20, 21].

The gamma-based approach originally proposed by Abgrall [11] and used by Terashima and Kawai [34] in the context of LAD schemes, is mathematically equivalent to the five-equation approach assuming single gas phase fluids are present only. In particular, for gamma-based approaches, the conservation equations for (total) density, partial mass fractions (ρ and $\rho Y^{(k)}$), and the transport equations for specific functions of γ entering the equation of state must be solved. If needed, the volume fraction can be computed as long as there are only two components with different values of γ [11, 10]. In the current study, these concepts are combined with the approach of Terashima and Kawai [34] and incorporates the stiffened gas equation of state and five-equation model, where the conservation and transport equations are written in terms of component's density and volume fraction ($\rho^{(k)}\alpha^{(k)}$ and $\alpha^{(k)}$) [37].

It is important to mention that following other studies [15, 36, 37, 9, 10] the source term related to the compressibility of the multiphase mixture (a term that implies gas volume fraction increases (decreases) across rarefaction (compression) waves) has been neglected. This assumption corresponds to the limit of infinite resolution and that the model tends toward the NavierStokes equations in each pure fluid and their coupling is only modeled across the interfaces. It is also important to note that this assumption limits the model to two-phase flows between pure fluids, which is the objective of the current approach [36].

In interface capturing methods, the volume fraction advection equation in the current non-conservative form could be used to advect equation of state parameters, such as $1/(\gamma-1)$ [9]. In this respect, appropriate mixture rules are required to prevent oscillations at the interface for velocity, pressure, and temperature [15, 38, 10]. These mixture rules, however, may vary based upon the EOS that is used.

2.2. *Stiffened gas EOS*

In this work, the stiffened gas EOS proposed by Le Métayer et al. [39] is employed. This EOS provides an accurate and simple model for the simulation of compressible flows with interfaces and has been validated against experiments [40]. With this model, the specific internal energy is related to the pressure and density via:

$$e(p,\rho) = \frac{p+\gamma B}{(\gamma-1)\rho} + q, \tag{4}$$

or to the temperature and pressure via:

$$e(p,T) = \frac{p+\gamma B}{p+B} cT + q, \tag{5}$$

where γ, B, c, and q are fitting parameters to experimental data. Each fluid takes its own fitting parameters (see Table I for a list of materials) and thus, this relation is valid for each phase (gas, liquid or solid) everywhere in the domain except inside interfaces.

2.3. *Mixture rules*

Mixture rules are used to calculate fluid properties inside interface regions. Pressure and temperature calculations in each phase are straightforward as properties associated with the respective phase are constant. However, caution needs to be exercised inside the interface to avoid oscillations in this region. The errors associated with improper calculation of pressure and temperature have been studied extensively in the literature [15, 36, 38]. These analyses use the mechanical equilibrium assumption [15]: "*if an interface evolves under uniform pressure, and velocity conditions, pressure, and velocity must remain uniform during time evolution*". These studies show that to find an oscillation-free interface, ρq and ρc need to transport conservatively via the equation for $\rho^{(k)}\alpha^{(k)}$

Table I. Thermo-physical stiffened gas EOS properties [10, 9]

	γ	$B(GPa)$	$q(kJ/kg)$	$c(kJ/kgK)$	$a_0(m/s)$
Air	1.4	0	0	0.718	343
Water ($O(10^2)$ MPa)	6.12	0.343	0	4.184	1450
Water ($O(10)$ GPa)	2.35	1	-1.167	1.816	2097
Helium	1.67	0	0	3.12	1008

and $1/(\gamma-1)$, $\gamma B/(\gamma-1)$, and B non-conservatively via the transport equation for $\alpha^{(k)}$. In other words, the properties entering the EOS (γ, B, c, Q) need to be calculated using

$$\frac{1}{\gamma-1} = \sum_k \alpha^{(k)} \left(\frac{1}{\gamma^{(k)}-1} \right), \tag{6a}$$

$$\frac{\gamma B}{\gamma-1} = \sum_k \alpha^{(k)} \left(\frac{\gamma^{(k)} B^{(k)}}{\gamma^{(k)}-1} \right), \tag{6b}$$

$$B = \sum_k \alpha^{(k)} B^{(k)}, \tag{6c}$$

$$\rho q = \sum_k \rho^{(k)} \alpha^{(k)} q^{(k)}, \tag{6d}$$

$$\rho c = \sum_k \rho^{(k)} \alpha^{(k)} c^{(k)}, \tag{6e}$$

where $\rho^{(k)}\alpha^{(k)}$ and $\alpha^{(k)}$ are calculated using Eq. 1a and 1d and the total density (ρ) as previously mentioned.

2.4. *Speed of sound*

The speed of sound is needed to solve the hyperbolic system of equations. Périguad et al. [36] used a convex average of sound speeds in each phase, which for the form of EOS used in this study and mixture quantities described in Sec. 2.3, the speed of sound is calculated using

$$\rho a^2 = \gamma B + \gamma p, \tag{7}$$

where the terms γ and γB are calculated using Eq. 6a and 6b.

2.5. *Euler equations with artificial diffusivity terms*

The goal is to use central schemes to model compressible fluids that share interfaces. Central finite differences are not generally stable in this respect due to the jump conditions in pressure, density and volume fraction. To regularize interfaces and shock waves across a number of grid points and to evolve the simulation stably, artificial diffusivity terms are added to the right-hand side of equations explicitly. If transport terms are eliminated, the mathematical model including the terms to capture interfaces and shock waves may be written

$$\frac{\partial \rho^{(k)}\alpha^{(k)}}{\partial t} + \frac{\partial}{\partial x_j}(\rho^{(k)}\alpha^{(k)}u_j) = \frac{\partial F_j^{\rho^{(k)}\alpha^{(k)}}}{\partial x_j}, \tag{8a}$$

$$\frac{\partial \rho u_i}{\partial t} + \frac{\partial}{\partial x_j}(\rho u_i u_j + p\delta_{ij}) = \frac{\partial F_j^{\rho u_i}}{\partial x_j} + R^{sh}_{\rho u_i}, \tag{8b}$$

$$\frac{\partial \rho e_t}{\partial t} + \frac{\partial}{\partial x_j}\left(u_j(\rho e_t + p)\right) = \frac{\partial F_j^{\rho e_t}}{\partial x_j} + R^{sh}_{\rho e_t}, \tag{8c}$$

$$\frac{\partial \alpha^{(k)}}{\partial t} + u_j\frac{\partial \alpha^{(k)}}{\partial x_j} = \frac{\partial F_j^{\alpha^{(k)}}}{\partial x_j}, \tag{8d}$$

where $F_j^{\rho^{(k)}\alpha^{(k)}}$, $F_j^{\rho u_j}$, $F_j^{\rho e_t}$, and $F_j^{\alpha^{(k)}}$ are artificial diffusion fluxes applied to the Euler equations to capture fluid interfaces only. These flux terms are found in Sec. 3 and localized to interfaces using the LAD scheme in Sec. 4.2.2. Additionally, $R^{sh}_{\rho u_i}$ and $R^{sh}_{\rho e_t}$ are artificial diffusivity terms to regularize shock waves. A typical LAD scheme has been employed [41] which is discussed briefly in Sec. 4.2.1.

3. CONSISTENT INTERFACIAL ARTIFICIAL DIFFUSION (AD) TERMS

In this section, consistent interfacial AD terms are derived for the simulation of compressible multicomponent/multiphase flows. The focus is on interfaces of fluids advecting under constant velocity and pressure in which the mechanical equilibrium condition holds across the interface, i.e. the closure model is $[u_j] = 0$, and $[p] = 0$. These conditions may change if mechanical equilibrium conditions are adjusted inside the interface, such as when surface tension is present.

3.1. AD terms for phase density and volume fraction

AD terms for density and volume fraction conservation equations are used as a basis to derive consistent terms for other equations. With the assumption of an interface advecting under constant pressure and velocity, density and volume fraction (Eq. 8a and 8d) can be rewritten in the following semi-discrete form:

$$\frac{d(\rho^{(k)}\alpha^{(k)})}{dt} + u_j D_j(\rho^{(k)}\alpha^{(k)}) = D_j(F_j^{\rho^{(k)}\alpha^{(k)}}), \tag{9a}$$

$$\frac{d\alpha^{(k)}}{dt} + u_j D_j(\alpha^{(k)}) = D_j(F_j^{\alpha^{(k)}}), \tag{9b}$$

where D_j is a linear operator representing any central discretization scheme used for the advection terms. The velocity, u_j, is taken out of derivatives because of the equilibrium condition (i.e. continuity of the velocity across the interface).

The total density (ρ) is the summation of all component densities. It follows that a consistent AD flux for total density is the summation of all AD density fluxes for each phase. This may also be deduced once total mass conservation equation is written in semi-discrete form,

$$\frac{d\rho}{dt} + u_j D_j(\rho) = D_j(F_j^{\rho}), \tag{10}$$

and from Eq. 9a the following relation holds:

$$F_j^{\rho} = \sum_k F_j^{\rho^{(k)}\alpha^{(k)}}. \tag{11}$$

3.2. Momentum equation

Following the same approach, the momentum equation is written in semi-discrete form (in the absence of any other force applied to the fluid volume, $f_j = 0$),

$$u_i \frac{d\rho}{dt} + u_j u_i D_j(\rho) = D_j(F_j^{\rho u_i}), \tag{12}$$

in which $D_j(p) = 0$ because $[p] = 0$. It is then clear that the right-hand side of the above equation divided by u_i is equal to the right-hand side of Eq. 10, or

$$F_j^{\rho u_i} = u_i \sum_k F_j^{\rho^{(k)}\alpha^{(k)}} = u_i F_j^{\rho}. \tag{13}$$

In other words, in order to properly diffuse the momentum equation at the interface, the AD terms need to be the summation of fluxes applied to each individual component's density equation times the local velocity.

3.3. Energy equation

First, the relation for internal energy (Eq. 6a, 6b and 4) is rewritten with the isobaric assumption

$$\rho e = p \sum_k \alpha^{(k)} \left(\frac{1}{\gamma^{(k)} - 1}\right) + \sum_k \alpha^{(k)} \left(\frac{\gamma^{(k)} B^{(k)}}{\gamma^{(k)} - 1}\right) + \sum_k \rho^{(k)} \alpha^{(k)} q^{(k)}, \tag{14}$$

which combined with $\rho e_t = \rho e + \frac{1}{2}\rho u_j u_j$ and the conservation equation for the total energy, yields

$$\frac{d}{dt}(\rho e + \frac{1}{2}\rho u_i u_i) + u_j D_j(\rho e + \frac{1}{2}\rho u_i u_i + p) = D_j(F_j^{\rho e_t}). \tag{15}$$

Using Eq. 6a, 6b and 4, and the assumptions $[u_j] = 0$ and $[p] = 0$, the above equation can be rewritten

$$\begin{aligned} &p\frac{d}{dt}\left[\sum_k \alpha^{(k)}\left(\frac{1}{\gamma^{(k)}-1}\right)\right] + \frac{d}{dt}\left[\sum_k \alpha^{(k)}\left(\frac{\gamma^{(k)}B^{(k)}}{\gamma^{(k)}-1}\right)\right] + \frac{d}{dt}\left[\sum_k \rho^{(k)}\alpha^{(k)}q^{(k)}\right] \\ &+ \frac{1}{2}u_i u_i\frac{d\rho}{dt} + u_j p D_j\left[\sum_k \alpha^{(k)}\left(\frac{1}{\gamma^{(k)}-1}\right)\right] + u_j D_j\left[\sum_k \alpha^{(k)}\left(\frac{\gamma^{(k)}B^{(k)}}{\gamma^{(k)}-1}\right)\right] \\ &+ u_j D_j\left[\sum_k \rho^{(k)}\alpha^{(k)}q^{(k)}\right] + \frac{1}{2}u_j u_i u_i D_j(\rho) = D_j(F_j^{\rho e_t}), \end{aligned} \tag{16}$$

which is true for each phase at all locations. The above equation breaks down to four sub-equations so that the AD flux $F_j^{\rho e_t}$ is the summation of AD terms for each sub-equation. To clarify this, these sub-equations are rewritten here with their corresponding AD terms,

$$p\frac{d}{dt}\left[\sum_k \alpha^{(k)}\left(\frac{1}{\gamma^{(k)}-1}\right)\right] + u_j p D_j\left[\sum_k \alpha^{(k)}\left(\frac{1}{\gamma^{(k)}-1}\right)\right] = D_j(F_j^{\rho e_t(1)}), \tag{17a}$$

$$\frac{d}{dt}\left[\sum_k \alpha^{(k)}\left(\frac{\gamma^{(k)}B^{(k)}}{\gamma^{(k)}-1}\right)\right] + u_j D_j\left[\sum_k \alpha^{(k)}\left(\frac{\gamma^{(k)}B^{(k)}}{\gamma^{(k)}-1}\right)\right] = D_j(F_j^{\rho e_t(2)}), \tag{17b}$$

$$\frac{d}{dt}\left[\sum_k \rho^{(k)}\alpha^{(k)}q^{(k)}\right] + u_j D_j\left[\sum_k \rho^{(k)}\alpha^{(k)}q^{(k)}\right] = D_j(F_j^{\rho e_t(3)}), \tag{17c}$$

$$\frac{1}{2}u_i u_i\frac{d\rho}{dt} + \frac{1}{2}u_j u_i u_i D_j(\rho) = D_j(F_j^{\rho e_t(4)}). \tag{17d}$$

Since $\left(\frac{1}{\gamma^{(k)}-1}\right), \left(\frac{\gamma^{(k)}B^{(k)}}{\gamma^{(k)}-1}\right)$, and $q^{(k)}$ are constant for each phase (k), using Eq. 9a and 9b, AD fluxes for each sub-equation can be written

$$F_j^{\rho e_t(1)} = p\sum_k \left(\frac{1}{\gamma^{(k)}-1}\right) F_j^{\alpha^{(k)}}, \tag{18a}$$

$$F_j^{\rho e_t(2)} = \sum_k \left(\frac{\gamma^{(k)}B^{(k)}}{\gamma^{(k)}-1}\right) F_j^{\alpha^{(k)}}, \tag{18b}$$

$$F_j^{\rho e_t(3)} = \sum_k q^{(k)} F_j^{\rho^{(k)}\alpha^{(k)}}, \tag{18c}$$

$$F_j^{\rho e_t(4)} = \frac{1}{2}u_i u_i F_j^{\rho}. \tag{18d}$$

Finally, the summation of all above terms gives the energy equation AD flux

$$F_j^{\rho e_t} = \left[\sum_k \left(\frac{p}{\gamma^{(k)}-1} + \frac{\gamma^{(k)}B^{(k)}}{\gamma^{(k)}-1}\right) F_j^{\alpha^{(k)}}\right] + \left[\sum_k q^{(k)} + \frac{1}{2}u_i u_i\right] F_j^{\rho}. \tag{19}$$

It is important to note that 19 is specialized to the EOS given in the Sec. 2. Other forms of EOS like Mie–Grüneisen [14] or Tait [42] would require different energy diffusion fluxes to be developed.

3.4. Summary of interfacial AD fluxes

The results of the above derivations are summarized for the momentum and energy equations:

$$\begin{bmatrix} F_j^{\rho u_i} \\ F_j^{\rho e_t} \end{bmatrix} = \begin{bmatrix} u_j F_j^{\rho} \\ (Q+K)F_j^{\rho} + (p\Gamma + \Pi)F_j^{\alpha^{(k)}} \end{bmatrix} \tag{20}$$

where $F_j^{\rho} = \sum_k F_j^{\rho^{(k)}\alpha^{(k)}}$, $Q = \sum_k q^{(k)}$, $K = \frac{1}{2}u_i u_i$, $\Gamma = \sum_k 1/(\gamma^{(k)} - 1)$, and $\Pi = \sum_k \gamma^{(k)} B^{(k)}/(\gamma^{(k)} - 1)$. The fluxes $F_j^{\rho^{(k)}\alpha^{(k)}}$ and $F_j^{\alpha^{(k)}}$ are found in Sec. 4.2.2, where they are combined with shock capturing diffusion fluxes to describe the entire mathematical model described in Sec. 2.5.

4. NUMERICAL IMPLEMENTATION

4.1. Spatial derivatives and time integration

AD fluxes in the previous section are valid for any central scheme, including high-order explicit and compact central finite differencing schemes [43, 32, 44]. In this work, the spatial derivatives are evaluated using central sixth-order finite differencing. Close to boundaries, one-sided differencing is used.

A third-order $O(\Delta t^3)$, fully explicit TVD Runge-Kutta (RK) time integration scheme advances the solution $\mathbf{U}^n$ to the next time step using [45]

$$\begin{aligned} \mathbf{U}^* &= \mathbf{U}^n + \Delta t \mathbf{F}(\mathbf{U}^n), \\ \mathbf{U}^{**} &= \frac{3}{4}\mathbf{U}^n + \frac{1}{4}\mathbf{U}^* + \frac{1}{4}\Delta t \mathbf{F}(\mathbf{U}^*), \\ \mathbf{U}^{n+1} &= \frac{1}{3}\mathbf{U}^n + \frac{2}{3}\mathbf{U}^{**} + \frac{2}{3}\Delta t \mathbf{F}(\mathbf{U}^{**}), \end{aligned} \tag{21}$$

where $\mathbf{U}^*$ and $\mathbf{U}^{**}$ represent the solution vector at an intermediate time stage and $\mathbf{F}(\mathbf{U})$ is the right-hand side of equations calculated using local solution vector $\mathbf{U}$. The convective-acoustic Courant-Friedrichs-Lewy (CFL) is defined as following:

$$CFL = \left(\sum_j^{dim} \frac{|u_j|}{\Delta x_j} + a \sqrt{\sum_j^{dim} \frac{1}{\Delta x_j^2}} \right) \Delta t, \tag{22}$$

where u is the local absolute velocity of the fluid and the speed of sound, a, is calculated using Eq. 7 for multiphase flow simulations. In all simulations, Δt is adaptively set to satisfy the advection constraint, with a CFL number of 0.45. This conservative CFL number provides both accuracy and stability. Although it has been noted in other work [32] that the magnitude of artificial diffusion can be significant when using stretched anisotropic grids and thus restrict the time stepping, this is not the case in this work.

Following the work of Cook et al. [29, 46] in the context of LAD schemes and high-order central methods, an eighth-order low-pass spatial filtering scheme is used after each RK step. This filtering scheme is important to ensure numerical stability. One-sided formulas are used for the points close to boundaries. In the filtering scheme, there is a free parameter in which the standard value of 0.495 is used. The properties of the filtering scheme are detailed in [47, 48].

4.2. Localized artificial diffusivity: LAD scheme

It is desirable to maintain high accuracy in regions where the solution is smooth and at the same time maintain stability at discontinuities. To accomplish this goal in the framework of central schemes, localized artificial diffusion is added to the flow field. These schemes have been designed to work with high-order central schemes (usually greater than 4th) in an attempt to capture the smallest scales [27, 29, 32].

Here, the LAD approach to capture shock waves [33] and contacts with density differences is extended to multiphase flows using the AD fluxes obtained in the previous section. The proposed artificial diffusion terms maintain equilibrium across the multiphase fluid interfaces with varying densities. Thus, in the presence of shock waves, regular numerical diffusion terms for shock capturing are required.

4.2.1. LAD for shock capturing The initial work of Cook [29] on artificial fluid properties for large-eddy simulations of compressible turbulence mixing is central to understanding LAD schemes. In order to damp out high wavenumber modes, at or close to the resolution limit, without corrupting lower modes, artificial fluid properties are added locally. The scheme is refined further by Mani et al. [41] and is being commonly referred to as the LES of turbulent flows with shocks. Following the same approach, grid-dependent artificial fluid transport coefficients are introduced. Using the same notation in Sec. 2.5, the artificial terms to capture shock waves are:

$$\begin{aligned} R^{sh}_{\rho u_i} &= \frac{\partial\left(\mu_\beta(\nabla_k u_k)\delta_{ij}\right)}{\partial x_j}, \\ R^{sh}_{\rho e_t} &= \frac{\partial\left(\mu_\beta(\nabla_k u_k)u_i\delta_{ij}\right)}{\partial x_j}, \end{aligned} \tag{23}$$

where $\nabla_k = \partial/\partial x_k$ is a partial derivative operator, δ_{ij} is the identity tensor and the spatial derivatives are calculated using a central difference scheme. The coefficient of artificial bulk viscosity, which localizes diffusion to shocks only is

$$\mu_\beta = C_\beta \rho \mathbf{H}(-\nabla_k u_k)\overline{\left|\sum_{l=1}^{dim}\frac{\partial^r(\nabla_k u_k)}{\partial x_l^r}\Delta^{r+2}\right|}, \tag{24}$$

where $r = 4$, $\Delta = (\Delta x \Delta y \Delta z)^{1/3}$ corresponds to the local grid spacing (for uniform grids $\Delta = \Delta x = \Delta y = \Delta z$) and $\mathbf{H}$ is a Heaviside function that limits diffusion to shock waves (and not expansion waves) [41]. The overbar indicates an approximate truncated Gaussian filter (see [27, 29] for more details).

Numerical experiments show that for the given spatial discretization and filtering scheme in this work, $C_\beta = 1.0$ is sufficient to capture a wide range of pressure ratios. Primary tests were performed on a gas-gas Riemann problem with pressure ratios ranging from 2 to 20. Additionally, the Shu-Osher problem [45] was solved to verify the shock-capturing scheme behaves appropriately. Figure 1 shows the density profile after a shock wave impacts the entropy wave (density fluctuations). For this case, the correct location and magnitude of the post-shock density waves have been captured. There is good agreement with the resolved WENO-5 simulation where there are no observed spurious oscillations. As noted in other work [30] the deviation from the WENO-5 simulation located at $x = -2.9$ on the right plot is purely an artifact of the initial condition.

4.2.2. LAD scheme for interfacial flows Diffusion fluxes for material interfaces must be localized to the interface itself. As shown in Sec. 3, when diffusion fluxes for density and volume fraction are constructed, consistent fluxes are created for momentum and energy equations. Thus, the extension of the LAD scheme to capture interfaces is straightforward once appropriate fluxes are calculated and localized to interfaces. Numerical diffusion terms exist for multicomponent flows where the total density, mass fraction, and a dummy advection equation for the EOS parameter is solved [34]. However, for multiphase flows and the form of stiffened EOS used in this work, phase densities and volume fraction must be diffused. This form for constructing artificial fluid properties follows the work of [34, 49] for multicomponent fluids and extends the LAD scheme to multiphase flows. The diffusion fluxes are written

$$\begin{aligned} F_j^{\rho^{(k)}\alpha^{(k)}} &= \beta_\rho^{(k)}\frac{\partial \rho^{(k)}\alpha^{(k)}}{\partial x_j}, \\ F_j^{\alpha^{(k)}} &= \beta_\alpha^{(k)}\frac{\partial \alpha^{(k)}}{\partial x_j}, \end{aligned} \tag{25}$$

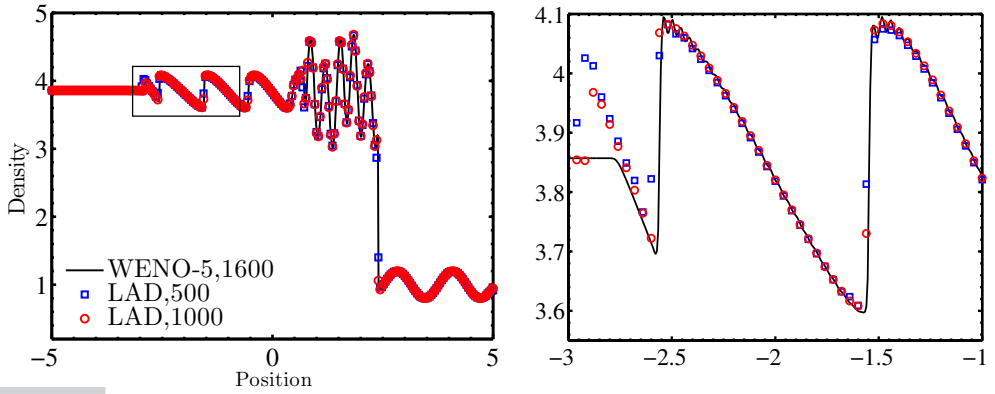

Figure 1. Solution to the Shu-Osher problem (left) and the zoomed-in area (right).

where $\beta_\rho^{(k)}$ and $\beta_\alpha^{(k)}$ are the coefficients for the artificial fluid properties for density and volume fractions. $\beta_\rho^{(k)}$, which localizes the diffusion to locations where density gradients exist, is defined

$$\beta_\rho^{(k)} = C_\rho \mathbf{H}(|\alpha^{(k)}(1-\alpha^{(k)})|)\frac{a}{\rho}\left|\sum_{l=1}^{dim}\frac{\partial^r \rho^{(k)}\alpha^{(k)}}{\partial x_l^r}\Delta^{r+1}\right|. \tag{26}$$

A similar equation was used by Terashima et al. [34] to localize diffusion to a gas-gas interface in a compressible two-component flow simulation. However, the approach used in their study did not use the Heaviside function, which is necessary to localize the diffusion to the interface alone.

$$\begin{aligned}\beta_\alpha^{(k)} = C_{1\alpha} a\left|\sum_{l=1}^{dim}\frac{\partial^r \alpha^{(k)}}{\partial x_l^r}\Delta^{r+1}\right| \\ + C_{2\alpha} a\Delta\left([\alpha^{(k)}-1]\mathbf{H}(\alpha^{(k)}-1) - \alpha^{(k)}[1-\mathbf{H}(\alpha^{(k)})]\right),\end{aligned} \tag{27}$$

where the first term ensures that diffusion is being added locally to the interface only and the second term becomes non-zero when the volume fraction goes above or below zero. The second term $\beta_\alpha^{(k)}$ bounds the volume fraction to the desired unity range $\alpha^{(k)} \in [0, 1]$.

Numerical experiments have shown that setting $C_\rho = C_{1\alpha} = 0.2$ and $C_{2\alpha} = 100$ results in a well-defined interface. The suggested values for the user-defined coefficient is a function of the spatial discretization and the filtering scheme. These values have been observed in this work to give reasonable results, but may change for other LAD implementations. In the limit that the grid spacing goes to zero (approaching continuum limit), the artificial fluid properties approach zero and will not affect the invariance of the governing equations.

For convenience, it is useful to derive simplified equations for a binary system, i.e. five-equation model, in a two-dimensional framework with the above AD terms. These equations are listed in A.

5. TEST PROBLEMS

The proposed LAD method is used to solve a variety of binary multicomponent and multiphase benchmark problems. To verify the effectiveness of the method, the LAD scheme is compared against analytical solutions (if available) and experimental data. The test cases presented in this paper are based on Eq. 1a, 1b, 1c, and 1d, where the Euler equations with artificial diffusion are presented.

For all problems, the acoustic CFL number is set to be 0.45 and the aforementioned values for user-defined constants in the LAD scheme are used. If not specified explicitly, problems are solved in a non-dimensional form by normalizing density and velocity with density and speed of sound in

ambient air, which is $\rho_{air} = 1.204\,\mathrm{kg/m^3}$ and $a_0 = 343\mathrm{m/s}$, respectively. In this way, the pressure and fitting parameter B are normalized with $\rho_0 a_0^2$. For water, the value for B that is $O(10^2)$ MPa has been used (see Table I) which is 2420 non-dimensional units.

Errors due to initial conditions remain undamped in high-order schemes. In order to minimize these errors, the interface is initialized over at least three points using a tangent hyperbola distribution.

5.1. 1-D Air-Water interface advection

Advection of a gas-liquid interface under constant velocity and pressure is a fundamental test case for multi-fluid flow. The outcome of this test illustrates the capability of the method to maintain velocity, pressure or temperature equilibrium at the interface as well as preventing overshoots that may contaminate the rest of the domain [9, 10]. This problem is also used to determine the impact of user-defined constants in the diffusion terms on the quality of the solution.

The advection test involves an air-water interface advecting under constant velocity, pressure and temperature in a domain $x \in [-1, 1]$ with periodic boundaries. The initial condition is expressed

$$(\rho_1\alpha_1, \rho_2\alpha_2, u, p, \alpha_1) = \begin{cases} (828.903, 0, 1, 1/\gamma_{air}, 1) & -1 \leq x \leq 0 \\ (0, 1, 1, 1/\gamma_{air}, 0) & 0 \leq x \leq 1. \end{cases} \tag{28}$$

Fig. 2 compares the solutions (after one period) in terms of volume fraction on a uniform grid with 100, 200 and 400 grid points given four different values of diffusion coefficient $C_{1\alpha} = 0.04, 0.2, 0.4, 1.0$ (Here $C_{2\alpha} = 0$). These results are used to calculate a maximum wiggle amplitude [43],

$$W_{max}(\%) = 100 \times \frac{max\left(|\alpha - 1|\mathbf{H}(\alpha - 1), |\alpha|\mathbf{H}(-\alpha)\right)}{\Delta\alpha}, \tag{29}$$

and a non-dimensional interface thickness

$$\frac{\delta}{\Delta x} = \frac{\Delta\alpha}{\Delta x \frac{\partial\alpha}{\partial x}}, \tag{30}$$

which represents the number of grid points across the interface.

Fig. 3 shows the maximum wiggle amplitude and interface thickness for different grid spacing and user-defined coefficients. It can be seen that maximum wiggle amplitude decreases with increasing model constant values. While the number of points used to resolve the interface increase with increasing resolution, overall about 3-5 points are necessary to resolve the interface. For $C_{1\alpha} = 0.2$, the normalized wiggle amplitude is approximately less than 0.3% and the interface (about 99% of the profile) is represented over 4 grid points. This range is acceptable for the simulations of interest in this paper. However, this may change if other differencing or filtering schemes are used.

Pressure and velocity remain constant in this problem. However, spurious oscillations may be produced at the interface due to the change in properties from the EOS. To check this condition, the error in these variables are plotted in Fig. 4. As it is shown in these plots, pressure, and velocity error are on the order of 10^{-11} and 10^{-12}, respectively. This shows that the proposed LAD scheme introduces minimal spurious oscillations at the interface and satisfies the equilibrium assumption.

The amplitude of maximum wiggles (which present the extent of oscillations in the solution) is inversely related to the grid spacing, which is common for high-order central schemes. Sufficient resolution along with the extra diffusion terms for over and undershoots (Eq. 29) minimizes oscillations across the interface to a reasonable level. An important aspect of the presented method is that the pressure equilibrium condition is not affected even in the presence of such small oscillations.

5.2. Stiff multi-phase Riemann problem

The gas-liquid Riemann problem is a simple model for an underwater explosion. This problem has been used as a benchmark test for the stiffened EOS in a variety of studies because it incorporates two-phase flows in a compressible configuration [50, 12, 9, 10]. Due to the stiffness of the problem, high-order schemes can introduce errors into the solution initially that remain undamped due to the

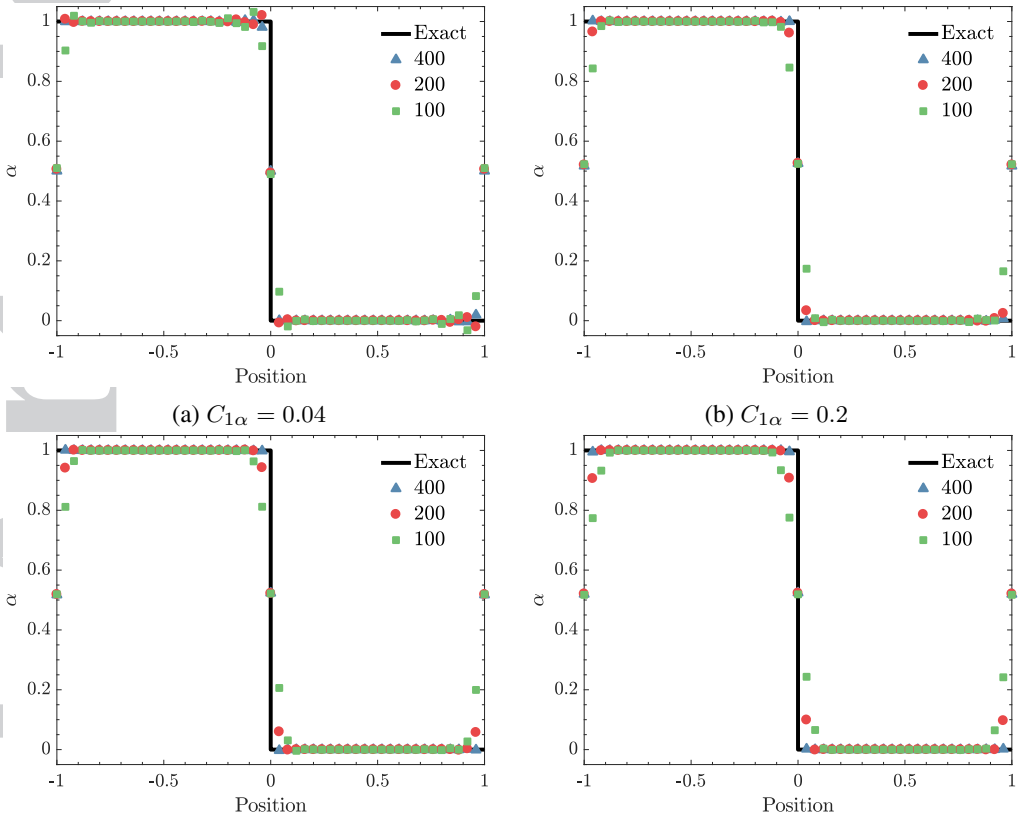

(a) $C_{1\alpha} = 0.04$ (b) $C_{1\alpha} = 0.2$

(c) $C_{1\alpha} = 0.4$ (d) $C_{1\alpha} = 1.0$

Figure 2. Solution to the gas-liquid advection problem after one period for four different user-defined diffusion coefficients and three different grid resolutions.

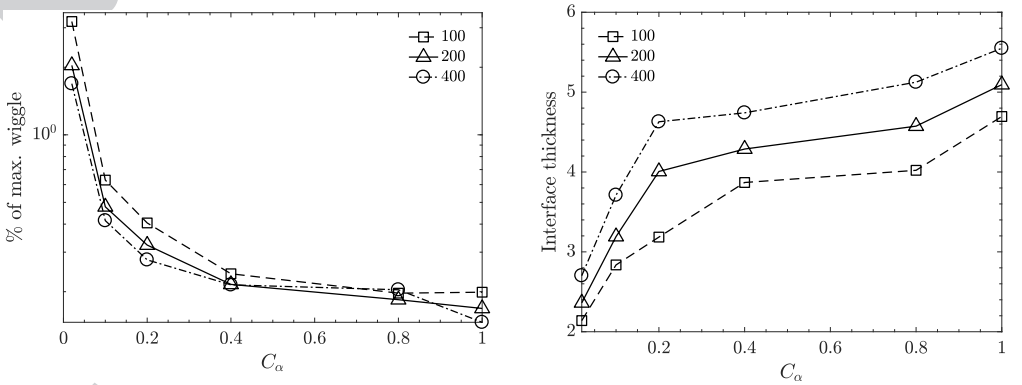

(a) Maximum wiggle amplitude (%) (b) Interface thickness

Figure 3. Maximum wiggle percentage and interface thickness versus user-defined diffusion coefficients for three grid resolutions.

lack of numerical diffusion. This test case also demonstrates the capability of the scheme to handle high pressure ratios.

At the initial condition, highly compressed air exists on the left and water at atmospheric pressure is on the right. The initial condition in non-dimensional form using the liquid as a reference state [9] (the reference values are $\rho_{ref} = 1007.064\ (kg/m^3)$ for density and $p_{ref} = 3269.16\ atm$ for

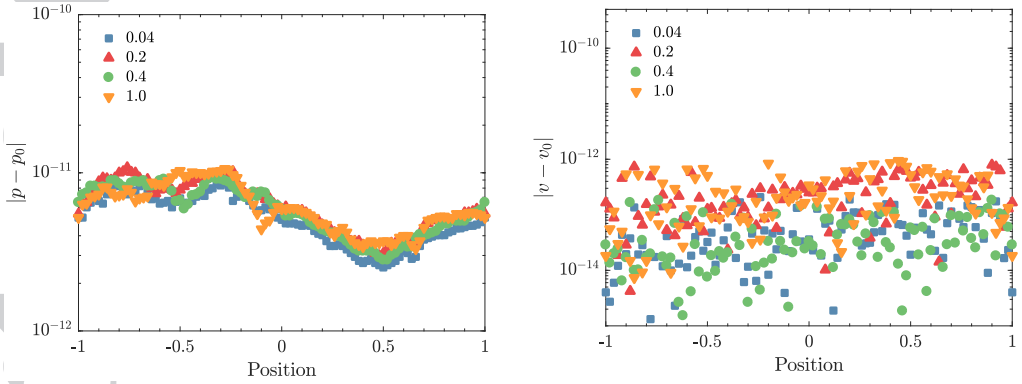

(a) Error in pressure

(b) Error in velocity

Figure 4. Pressure and velocity error for the 1-D advection problem after one period for different user-defined C_α coefficients.

Table II. Error and convergence order for different stencils (error is defined as $\sum_{i=1}^{N} |\rho_i - \rho_{i,analytical}|$).

No. of grids	Error	Order
200	4.6×10^{-3}	
400	2.6×10^{-3}	0.8261
600	1.9×10^{-3}	0.7752
800	1.5×10^{-3}	0.8229
1000	1.3×10^{-3}	0.6420

pressure) is given by:

$$(\rho_1\alpha_1, \rho_2\alpha_2, u, p, \alpha_1) = \begin{cases} (1.241, 0, 0, 2.573, 1) & -1 \leq x \leq 0, \\ (0, 0.991, 0, 3.059 \times 10^{-4}, 0) & 0 \leq x \leq 1, \end{cases} \tag{31}$$

Three grid sizes with 100, 500, and 2000 points are used to simulate this problem and the results obtained for total density, pressure, and volume fraction are compared with the exact solutions in Fig. 5. The discontinuity in the initial condition is smoothed over two grid points and the simulation is run until $t = 0.2$ (non-dimensional units). Although this is an extreme test case for any central scheme , the results suggest that the method is able to predict the correct location of the interface, transmitted shock wave, and expansion fan and the pressure remains constant across the interface as intended. Oscillations in pressure and density profiles are observed close to the tail of the expansion fan and the interface, respectively. As seen in Fig. 5, the order of these oscillations decreases significantly as the number of grid points increases and the density or pressure profiles match the given exact solution.

This problem is also used to demonstrate the convergence of the method. The absolute error and the order of convergence of this problem is plotted for different resolutions. Due to the assortment of discontinuities in this problem, it is not expected to be better than a first order accurate, which is clear from Table II.

5.3. 2-D advection of a water column

In this problem, a water cylinder with diameter $D = 1$ advects under constant pressure and velocity in a periodic two-dimensional domain. The initial condition is

$$(\rho_1\alpha_1, \rho_2\alpha_2, u, p, \alpha_1) = \begin{cases} (1, 0, 1, 1/\gamma_{air}, 1) & \text{air}, \\ (0, 828.903, 1, 1/\gamma_{air}, 0) & \text{water}, \end{cases} \tag{32}$$

where the computational domain is $5D \times 5D$ and there are 20 computational points across the diameter of the cylinder. This simple problem shows the benefits of high-order schemes in

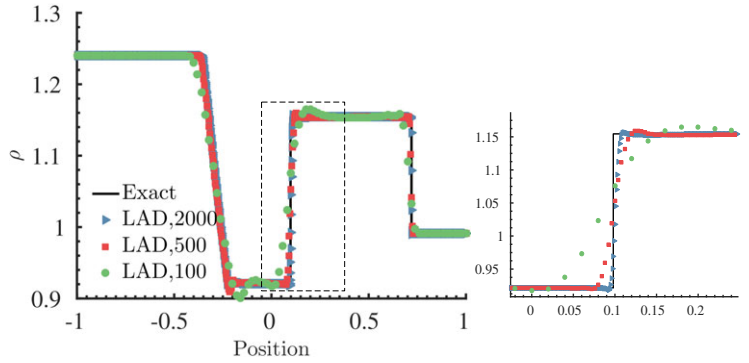

(a) Density

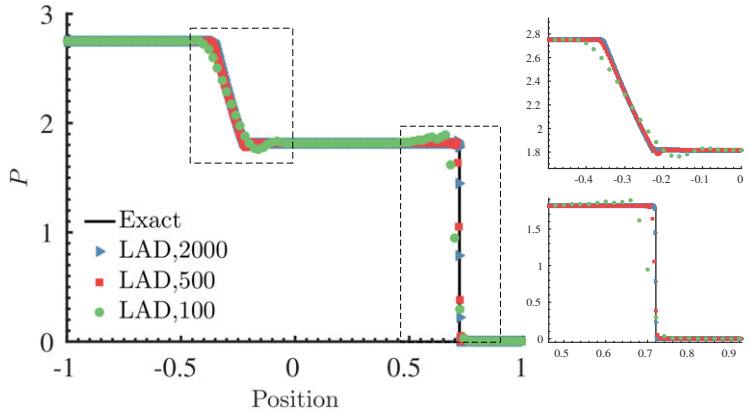

(b) Pressure

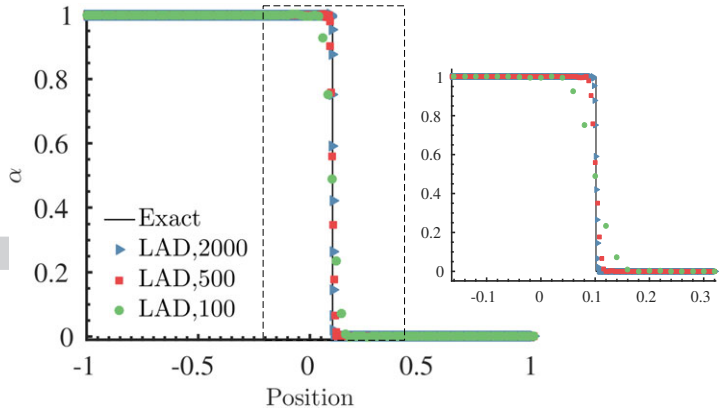

(c) Volume fraction

Figure 5. Solution to the gas-liquid Riemann problem at $t = 0.2$ for density, pressure, and volume fraction.

maintaining the spherically symmetric flow fields around a water column. Fig. 6 shows the iso-contours of volume fraction after one period of advection using the proposed LAD scheme and a multifluid solver which uses a second-order MUSCL reconstruction scheme with a HLLC Riemann solver following [37]. The cylinder remains circular and symmetric for the LAD scheme, however, clipping errors due to grid anisotropy cause the MUSCL scheme cylinder to appear stretched in the direction of motion (see Fig. 6). At least four times higher resolution is needed to achieve the same accuracy using second-order MUSCL. In a two-dimensional simulation, this number corresponds to a significant increase in computational time. It should be noted that other high-order schemes such

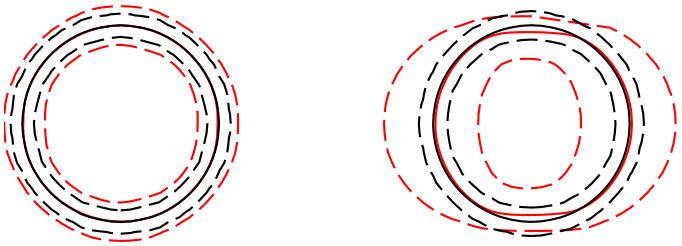

Figure 6. Iso-contours of volume fraction for the liquid cylinder advection problem using the proposed LAD scheme (left) and second-order MUSCL (right). The initial condition is plotted with black and the solution after one period is red. The middle line is defined as $\alpha_l = 0.5$ and the inner and outer dashed-lines are 0.99 and 0.01, respectively.

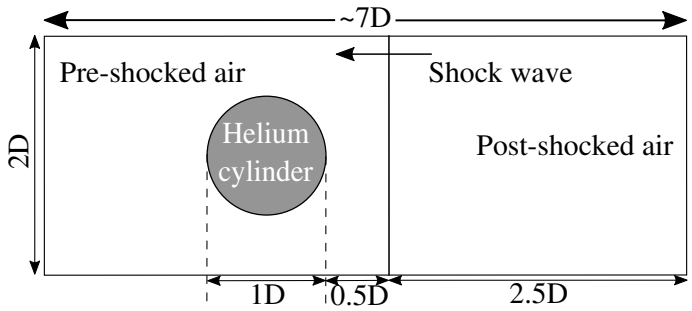

Figure 7. Schematic of the shock-helium bubble computational domain.

as WENO5 [9, 22] can also maintain shape preservation as demonstrated in [22] with a collapsing droplet.

5.4. 2-D shock-helium bubble interaction

A well-known [7, 34, 51, 46] multi-component test case is a helium cylindrical bubble interacting with a Mach 1.22 normal shock wave. Fig. 7 shows a schematic of the computational domain. The initial gas conditions for this case are

$$(\rho_1\alpha_1, \rho_2\alpha_2, u, p, \alpha_1) = \begin{cases} (1, 0, 0, 1/\gamma_{air}, 1) & \text{pre-shocked air,} \\ (1.3769, 0, -0.3336, 1.5698/\gamma_{air}, 1) & \text{post-shocked air,} \\ (0, 0.1819, 0, 1/\gamma_{air}, 0) & \text{helium bubble.} \end{cases} \tag{33}$$

The computational domain and the location of the cylinder and shock wave are given in Fig. 7. The left and right boundaries are extrapolated using the inside points and slip walls are used on the top and bottom. The problem is solved with three different grid sizes with 50, 100, and 200 points across the helium bubble.

The density gradient at $t = 0.6$ is shown in Fig. 8. As it can be seen, the scheme is able to resolve the complex twin reflected-refracted (TRR) shock structure, the side shock and the resulting expansion fan. It is important to capture the TRR structure because it is the primary mechanism for depositing baroclinic vorticity at the interface, which further downstream will cause folding of the interface and mixing.

Fig. 9 compares the numerical results to the experiments of Quirk and Karni [52] where good qualitative agreement is observed. Similar shock/expansion wave structures are observed in both the numerical simulation and experiment. Additionally, the compression and folding of the bubble interface shows a similar behavior as well.

To quantify the problem, the downstream and upstream location of the bubble and the air-jet penetrating into the bubble are tracked (see Fig. 10 for more details on these spots) and compared with the front tracking method of Terashima et al. [7, 34]. Good agreement is observed for both

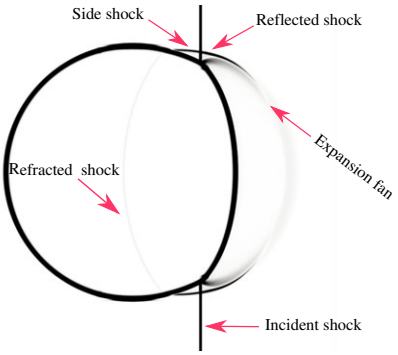

Figure 8. Gradient of density at $t = 0.6$ showing the structure of twin regular reflection-refraction (TRR)

the jet and downstream locations. The simulation upstream location appears slightly downstream, although the slope of the lines (which is the velocity of upstream location) matches closely.

5.5. *2-D shock-water cylinder interaction*

As a final demonstration of the method's ability to perform high-fidelity simulations, the interaction of a normal shock with a water column is presented. The full flow behavior includes multiple different physical processes such as surface tension and viscous forces that span a wide range of scales [53, 54]. However, since the objective is to demonstrate the capabilities of the existing method, the Euler equations are used and surface tension and viscous effects are ignored. Thus, only the early stages of droplet deformation may be captured after which these other forces become important. Fig. 11 shows the schematic of the computational domain. The domain is 22 diameters long in the x-direction and 10 diameters high in the y direction. For a Mach 1.47 shock wave in air and a water droplet in quiescent air, the initial conditions are

$$(\rho_1\alpha_1, \rho_2\alpha_2, u, p, \alpha_1) = \begin{cases} (1.0, 0, 0, 1/\gamma_{air}, 1) & \text{pre-shocked air,} \\ (1.810, 0, 0.658, 2.354/\gamma_{air}, 1) & \text{post-shocked air,} \\ (0, 820.903, 0, 1/\gamma_{air}, 0) & \text{water cylinder,} \end{cases} \tag{34}$$

where the reference values for density and velocity are $\rho_{air} = 1.204\,\mathrm{kg/m^3}$ and $a_{air} = 343\,\mathrm{m/s}$ respectively.

The simulation is performed with a grid of 2200×1000 cells, which gives 100 points across the diameter of the cylinder. Fig. 12 shows vorticity and pressure contours $46\,\mu$s after the shock reaches the water cylinder. Negative vorticity-stream on the top half (the bottom half has a positive vorticity-stream) of the cylinder is created due to misalignment of pressure and density gradients in the flow. As shown by the pressure contours, the vorticity is transported downstream and creates a clockwise recirculation region behind the cylinder. It can also be seen that a positive vorticity-stream is generated and moved up by the bigger negative vorticity. This recirculation region persists through the early deformation times. The observed results closely resemble that discussed in [56].

The numerical results are compared with the experiments of Igra and Takayama [55] in Fig. 13. Qualitative comparison shows that primary and secondary waves created by the interaction of the shock wave with the water column are captured accurately. Additionally, the numerical Schlieren image at $t = 43\,\mu$s shows clearly the formation of Mach reflections and slip lines from the edges of the droplet.

In order to analyze the droplet evolution, a sequence Schlieren and pressure contour plots are shown in Fig. 14 for two different grid sizes, which correspond to 40 and 80 grid points across the droplet diameter. As could be expected of a high-order scheme, the overall flow behavior is very similar to that observed in the WENO-5 results of Meng and Colonius [56]. More flow features are observed in the higher resolution case, however, the qualitative behavior of the breakup between the two cases is very similar. An unsteady recirculation region is formed behind the cylinders and a standing shock wave exists behind the water cylinder [56]. Due to the non-dissipative nature of the

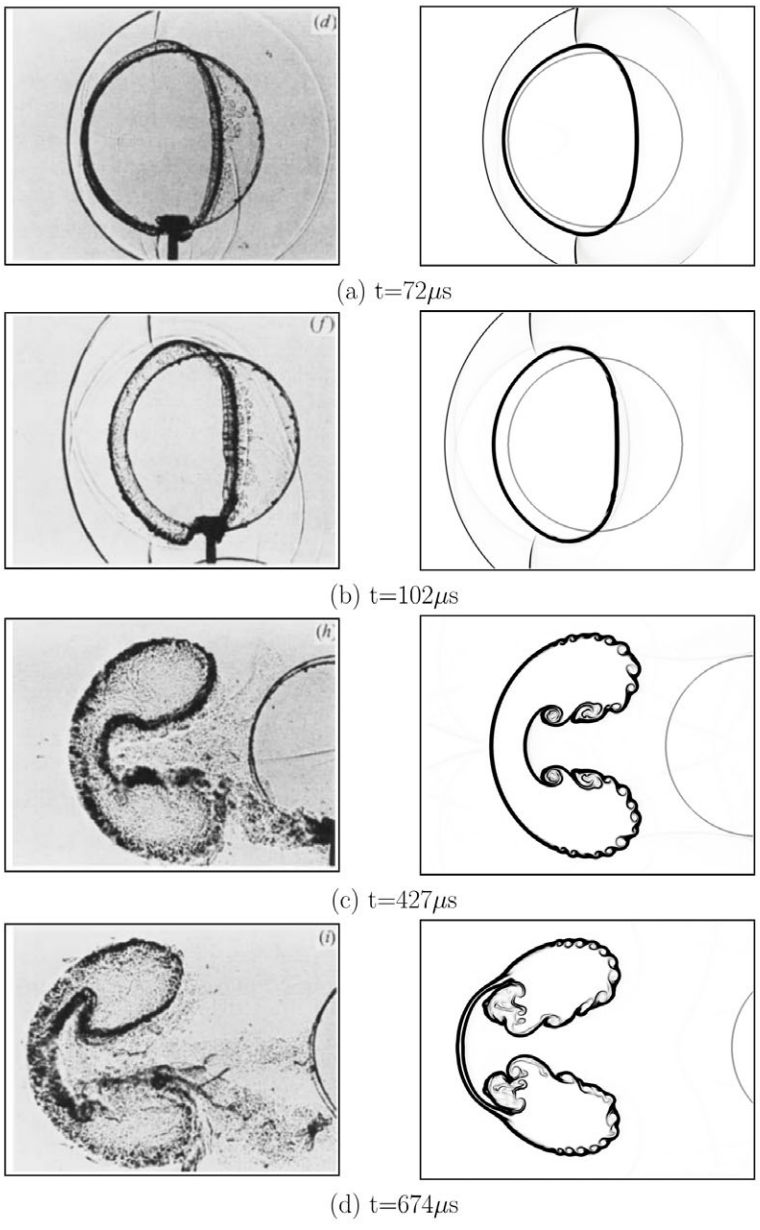

Figure 9. Snapshots from the Quirk and Karni experiment [52] (left) and numerical Schilieren images (right). Grey curves in the numerical images indicate the initial location of the Helium bubble.

numerical method, the small vortex structures do not dissipate and are transported downstream with the flow.

Unsteady drag coefficient of a droplet exposed to a high-speed flow is an important parameter in the large-scale modeling (for example, droplet cloud simulations). The drag coefficient (C_D) depends on the cylinder's center-of-mass velocity ($\bar{u}$) and acceleration ($\bar{a}$) through [56]

$$C_D = \frac{m\bar{a}}{\frac{1}{2}\rho_g(u_g - \bar{u})^2 d_0}, \tag{35}$$

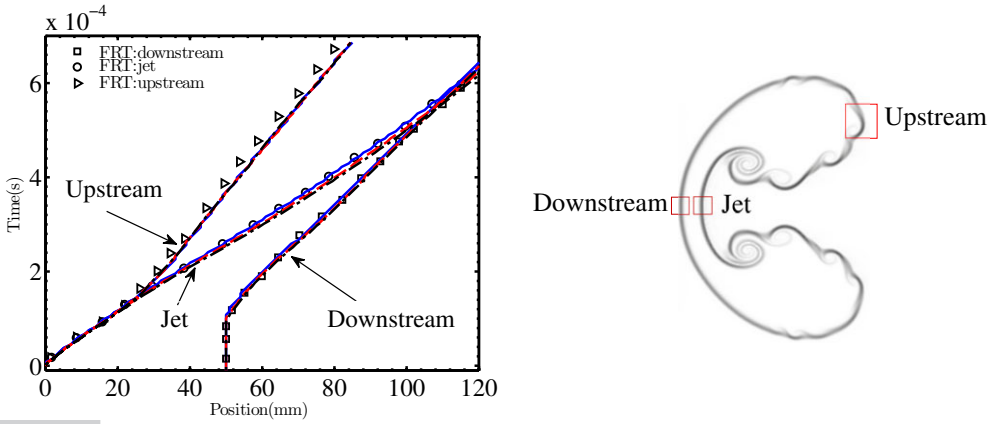

Figure 10. Left: jet, upstream and downstream locations of the helium bubble compared with the results in [7, 34]. The number of grid points for the solid line is 350×100, dashed line is 700×200, and dash-dotted line is 1400×400. A schematic of their location on the bubble is depicted on the right.

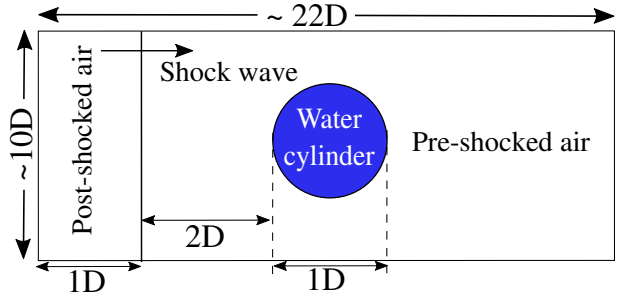

Figure 11. Schematic of the shock-water cylinder computational domain.

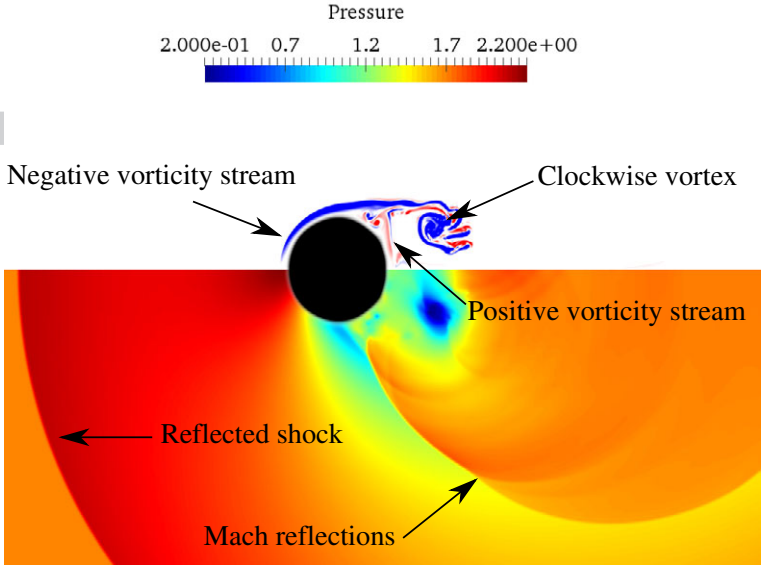

Figure 12. Vorticity (positive is red and negative is blue) on top and contours of pressure representing the wave structure on bottom for shock-water cylinder problem at $t = 46\ \mu$s.

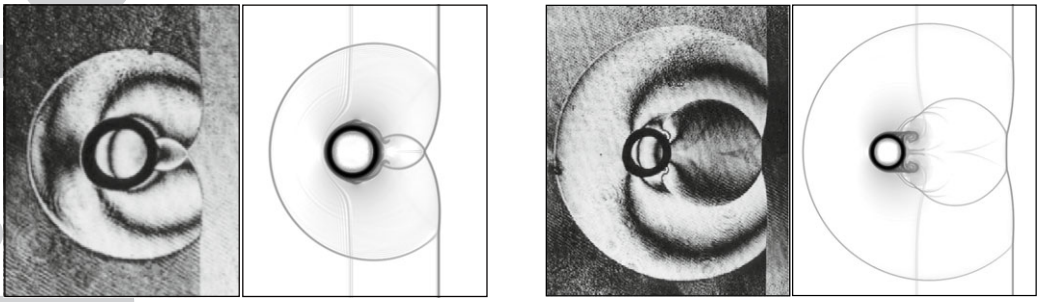

(a) t=23 μs (b) t=43 μs

Figure 13. Infinite fringe double exposure holographic interferograms of Igra and Takayama [55] (left) and numerical Schlieren (right) for the shock-water cylinder interaction. The initial incident time is used for reference or $t = 0$.

where m and d_0 are the constant mass and diameter of the water cylinder, ρ_g and u_g are the post-shock density and velocity of the air, and the center-of-mass velocity and acceleration are calculated using the liquid partial density ($\rho_2\alpha_2$)

$$\bar{u} = \frac{\int \alpha_2\rho_2 u dV}{\int \alpha_2\rho_2 dV}, \bar{a} = \frac{\frac{d}{dt}\int \alpha_2\rho_2 u dV}{\int \alpha_2\rho_2 dV}. \tag{36}$$

The evolution of the drag coefficient is plotted in Fig. 15 and compared with the study of Meng and Colonius [56] (t_a used in this figure is the non-dimensional acoustic time: $t_a = a_{air}t/D$). Initially the peak in the drag coefficient match very well but for $t_a > 1$ the results from Meng and Colonious are consistently higher than those observed in the present study. In their study, Meng and Colonious discuss the existence of a persistent upstream jet as an artifact of using symmetry in the simulation. However, in the present study, that does not assume symmetry, this upstream jet is significantly weaker and disappears quickly (see Fig. 14 b, c, and d). Once the upstream jet and recirculation area around the cylinder have disappeared ($t_a > 6$), the two solutions become quantitatively comparable. The appearance of asymmetry at late times, despite the perfectly symmetric initial conditions, are often observed in high-order simulation of Euler equations as well [17] due to accumulation of machine precision errors. Moreover, cylinder and droplet breakup show asymmetries during the late stages of breakup [56]. Also, due to the deformation of the cylinder in the later stages, an unsteady behavior of the drag coefficients is detected.

6. CONCLUSION

A new class of artificial diffusion methods is proposed to regularize the simulation of interfacial multiphase flows using the interface capturing approach. The system of equations is closed using a stiffened equation of state where the fluid interface is used to separate different components. Consistent and general forms of artificial diffusion fluxes are derived for volume fraction-based method with central difference schemes. These fluxes guarantee oscillation-free interface properties for pressure, velocity, and temperature. Extension to higher-order LAD methods is proposed and the analysis shows consistent application of these terms is required to maintain interface equilibrium. A variety of test problems illustrate the effectiveness of the method and the benefits of high-order accuracy. The multiphase LAD scheme accurately reproduces the salient features of liquid breakup early stages without being numerically complex and computationally cumbersome. Approved for public release: LA-UR-17-31324.

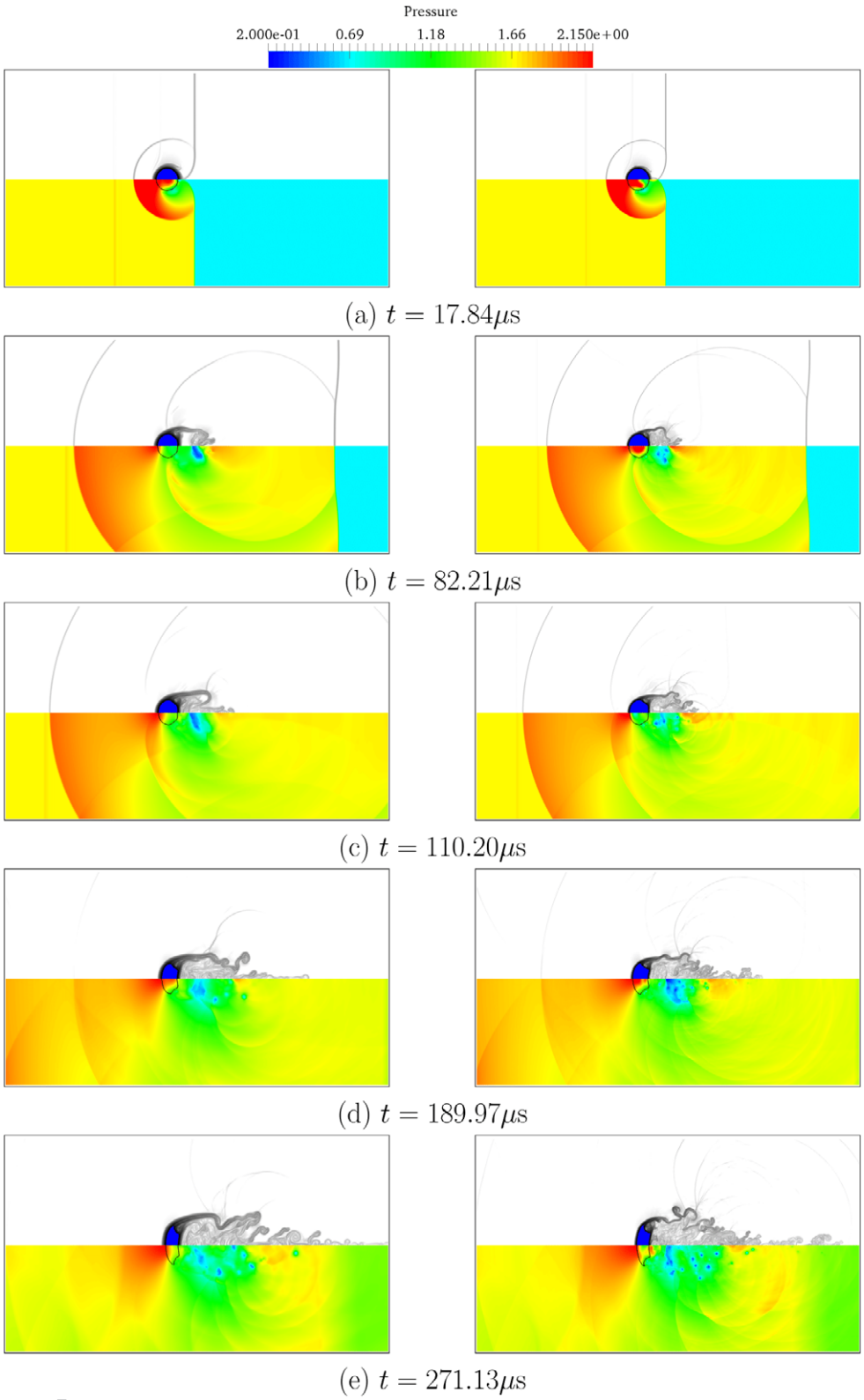

Figure 14. Numerical Schieleren (top) and filled pressure contours (bottom) for two grid sizes of 1100 on left and 2200×1000 on right. Blue iso-contours indicate $\alpha_l \geq 0.5$.

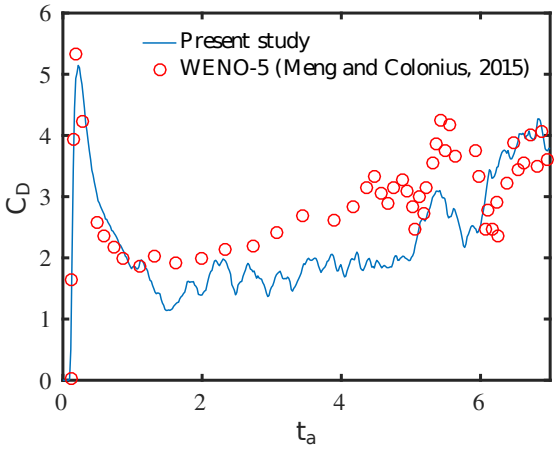

Figure 15. Unsteady drag coefficient for the shock-water column problem in Meng and Colonius [56] and the present study.

A. SIMPLIFIED EQUATIONS: TWO-FLUID MODEL IN 2D

To simplify the equations, q is set to zero, which can be done in conditions where temperature is not modeled. The properties for the first and second fluid are $(\gamma, B, q)^{(1)} = (\gamma_1, \pi_{\infty,1}, 0)$ and $(\gamma, B, q)^{(2)} = (\gamma_2, \pi_{\infty,2}, 0)$, respectively. The Euler equations with AD fluxes necessary to capture shock waves and consistent interfacial AD terms to maintain equilibrium across interfaces take the form

$$\frac{\partial \rho_1\alpha_1}{\partial t} + \frac{\partial}{\partial x}(\rho_1\alpha_1 u) + \frac{\partial}{\partial y}(\rho_1\alpha_1 v) = \frac{\partial F_x^{\rho_1\alpha_1}}{\partial x} + \frac{\partial F_y^{\rho_1\alpha_1}}{\partial y}, \tag{37a}$$

$$\frac{\partial \rho_2\alpha_2}{\partial t} + \frac{\partial}{\partial x}(\rho_2\alpha_2 u) + \frac{\partial}{\partial y}(\rho_2\alpha_2 v) = \frac{\partial F_x^{\rho_2\alpha_2}}{\partial x} + \frac{\partial F_y^{\rho_2\alpha_2}}{\partial y}, \tag{37b}$$

$$\frac{\partial \rho u}{\partial t} + \frac{\partial}{\partial x}(\rho u^2 + p) + \frac{\partial}{\partial y}(\rho uv) = \frac{\partial \left(uF_x^{\rho}\right)}{\partial x} + \frac{\partial \left(uF_y^{\rho}\right)}{\partial y} + R_{\rho u}^{shock} \tag{38a}$$

$$\frac{\partial \rho v}{\partial t} + \frac{\partial}{\partial y}(\rho v^2 + p) + \frac{\partial}{\partial x}(\rho uv) = \frac{\partial \left(vF_x^{\rho}\right)}{\partial x} + \frac{\partial \left(vF_y^{\rho}\right)}{\partial y} + R_{\rho v}^{shock} \tag{38b}$$

$$\begin{aligned}\frac{\partial \rho e_t}{\partial t} + \frac{\partial}{\partial x}\left(u(\rho e_t + p)\right) + \frac{\partial}{\partial y}\left(v(\rho e_t + p)\right) &= \frac{1}{2}\frac{\partial \left(F_x^{\rho}[u^2+v^2]\right)}{\partial x} + \frac{1}{2}\frac{\partial \left(F_y^{\rho}[u^2+v^2]\right)}{\partial y} \\ &+ \frac{\partial([p\Gamma + \Pi]\, F_x^{\alpha_1})}{\partial x} + \frac{\partial([p\Gamma + \Pi]\, F_y^{\alpha_1})}{\partial y} + R_{\rho e_t}^{shock}\end{aligned} \tag{39}$$

$$\frac{\partial \alpha_1}{\partial t} + u\frac{\partial \alpha_1}{\partial x} + v\frac{\partial \alpha_1}{\partial y} = \frac{\partial F_x^{\alpha_1}}{\partial x} + \frac{\partial F_y^{\alpha_1}}{\partial y} \tag{40}$$

where $F_x^{\rho_1\alpha_1}$, $F_x^{\rho_2\alpha_2}$, $F_x^{\alpha_1}$, $F_y^{\rho_1\alpha_1}$, $F_y^{\rho_2\alpha_2}$ and $F_y^{\alpha_1}$ are found using Eq. 25, $R_{\rho u}^{shock}$ and $R_{\rho v}^{shock}$, and $R_{\rho e_t}^{shock}$ are calculated using Eq. 23, and $\Gamma = \frac{1}{\gamma_1 - 1} - \frac{1}{\gamma_2 - 1}$, $\Pi = \frac{\gamma_1 \pi_{\infty,1}}{\gamma_1 - 1} - \frac{\gamma_2 \pi_{\infty,2}}{\gamma_2 - 1}$ and $\frac{\partial F_j^{\rho}}{\partial x_j} = \frac{\partial F_{x_j}^{\rho_1\alpha_1}}{\partial x_j} + \frac{\partial F_j^{\rho_2\alpha_2}}{\partial x_j}$.

REFERENCES

1. Osher S, Sethian JA. Fronts propagating with curvature-dependent speed: algorithms based on hamilton-jacobi formulations. *Journal of computational physics* 1988; **79**(1):12–49.
2. Fedkiw RP, Aslam T, Merriman B, Osher S. A non-oscillatory eulerian approach to interfaces in multimaterial flows (the ghost fluid method). *Journal of computational physics* 1999; **152**(2):457–492.
3. Osher S, Fedkiw RP. Level set methods: an overview and some recent results. *Journal of Computational physics* 2001; **169**(2):463–502.
4. Glimm J, Grove JW, Li XL, Shyue Km, Zeng Y, Zhang Q. Three-dimensional front tracking. *SIAM Journal on Scientific Computing* 1998; **19**(3):703–727.
5. Chern IL, Glimm J, McBryan O, Plohr B, Yaniv S. Front tracking for gas dynamics. *Journal of Computational Physics* 1986; **62**(1):83–110.
6. Glimm J, Li X, Liu Y, Xu Z, Zhao N. Conservative front tracking with improved accuracy. *SIAM Journal on Numerical Analysis* 2003; **41**(5):1926–1947.
7. Terashima H, Tryggvason G. A front-tracking/ghost-fluid method for fluid interfaces in compressible flows. *Journal of Computational Physics* 2009; **228**(11):4012–4037.
8. Liu T, Khoo B, Wang C. The ghost fluid method for compressible gas–water simulation. *Journal of Computational Physics* 2005; **204**(1):193–221.
9. Coralic V, Colonius T. Finite-volume weno scheme for viscous compressible multicomponent flows. *Journal of computational physics* 2014; **274**:95–121.
10. Beig SA, Johnsen E. Maintaining interface equilibrium conditions in compressible multiphase flows using interface capturing. *Journal of Computational Physics* 2015; **302**:548–566.
11. Abgrall R. How to prevent pressure oscillations in multicomponent flow calculations: a quasi conservative approach. *Journal of Computational Physics* 1996; **125**(1):150–160.
12. Shyue KM. An efficient shock-capturing algorithm for compressible multicomponent problems. *Journal of Computational Physics* 1998; **142**(1):208–242.
13. Shyue KM. A fluid-mixture type algorithm for compressible multicomponent flow with van der waals equation of state. *Journal of Computational Physics* 1999; **156**(1):43–88.

14. Shyue KM. A fluid-mixture type algorithm for compressible multicomponent flow with mie–grüneisen equation of state. *Journal of Computational Physics* 2001; **171**(2):678–707.
15. Allaire G, Clerc S, Kokh S. A five-equation model for the simulation of interfaces between compressible fluids. *Journal of Computational Physics* 2002; **181**(2):577–616.
16. Johnsen E, Colonius T. Implementation of weno schemes in compressible multicomponent flow problems. *Journal of Computational Physics* 2006; **219**(2):715–732.
17. Movahed P, Johnsen E. A solution-adaptive method for efficient compressible multifluid simulations, with application to the richtmyer–meshkov instability. *Journal of Computational Physics* 2013; **239**:166–186.
18. Kokh S, Lagoutiere F. An anti-diffusive numerical scheme for the simulation of interfaces between compressible fluids by means of a five-equation model. *Journal of Computational Physics* 2010; **229**(8):2773–2809.
19. So K, Hu X, Adams N. Anti-diffusion interface sharpening technique for two-phase compressible flow simulations. *Journal of Computational Physics* 2012; **231**(11):4304–4323.
20. Shukla RK, Pantano C, Freund JB. An interface capturing method for the simulation of multi-phase compressible flows. *Journal of Computational Physics* 2010; **229**(19):7411–7439.
21. Shukla RK. Nonlinear preconditioning for efficient and accurate interface capturing in simulation of multicomponent compressible flows. *Journal of Computational Physics* 2014; **276**:508–540.
22. Tiwari A, Freund JB, Pantano C. A diffuse interface model with immiscibility preservation. *Journal of computational physics* 2013; **252**:290–309.
23. Shyue KM, Xiao F. An eulerian interface sharpening algorithm for compressible two-phase flow: The algebraic thinc approach. *Journal of Computational Physics* 2014; **268**:326–354.
24. Garrick DP, Hagen WA, Regele JD. An interface capturing scheme for modeling atomization in compressible flows. *Journal of Computational Physics* 2017; .
25. Deng X, Inaba S, Xie B, Shyue KM, Xiao F. Implementation of bvd (boundary variation diminishing) algorithm in simulations of compressible multiphase flows. *arXiv preprint arXiv:1704.08041* 2017; .
26. Deng X, Inaba S, Xie B, Shyue KM, Xiao F. High fidelity discontinuity-resolving reconstruction for compressible multiphase flows with moving interfaces. *Journal of Computational Physics* 2018; .
27. Cook AW, Cabot WH. A high-wavenumber viscosity for high-resolution numerical methods. *Journal of Computational Physics* 2004; **195**(2):594–601.
28. Cook AW, Cabot WH. Hyperviscosity for shock-turbulence interactions. *Journal of Computational Physics* 2005; **203**(2):379–385.
29. Cook AW. Artificial fluid properties for large-eddy simulation of compressible turbulent mixing. *Physics of Fluids (1994-present)* 2007; **19**(5):055 103.
30. Johnsen E, Larsson J, Bhagatwala AV, Cabot WH, Moin P, Olson BJ, Rawat PS, Shankar SK, Sjögreen B, Yee H, *et al.*. Assessment of high-resolution methods for numerical simulations of compressible turbulence with shock waves. *Journal of Computational Physics* 2010; **229**(4):1213–1237.
31. Pirozzoli S. Numerical methods for high-speed flows. *Annual review of fluid mechanics* 2011; **43**:163–194.
32. Kawai S, Shankar SK, Lele SK. Assessment of localized artificial diffusivity scheme for large-eddy simulation of compressible turbulent flows. *Journal of Computational Physics* 2010; **229**(5):1739–1762.
33. Brehm C, Barad MF, Housman JA, Kiris CC. A comparison of higher-order finite-difference shock capturing schemes. *Computers & Fluids* 2015; **122**:184–208.
34. Terashima H, Kawai S, Koshi M. Consistent numerical diffusion terms for simulating compressible multicomponent flows. *Computers & Fluids* 2013; **88**:484–495.
35. Kapila A, Menikoff R, Bdzil J, Son S, Stewart DS. Two-phase modeling of deflagration-to-detonation transition in granular materials: Reduced equations. *Physics of Fluids (1994-present)* 2001; **13**(10):3002–3024.
36. Perigaud G, Saurel R. A compressible flow model with capillary effects. *Journal of Computational Physics* 2005; **209**(1):139–178.
37. Murrone A, Guillard H. A five equation reduced model for compressible two phase flow problems. *Journal of Computational Physics* 2005; **202**(2):664–698.
38. Johnsen E, Ham F. Preventing numerical errors generated by interface-capturing schemes in compressible multi-material flows. *Journal of Computational Physics* 2012; **231**(17):5705–5717.
39. Le Métayer O, Massoni J, Saurel R. Modelling evaporation fronts with reactive riemann solvers. *Journal of Computational Physics* 2005; **205**(2):567–610.
40. Saurel R, Petitpas F, Abgrall R. Modelling phase transition in metastable liquids: application to cavitating and flashing flows. *Journal of Fluid Mechanics* 2008; **607**:313–350.
41. Mani A, Larsson J, Moin P. Suitability of artificial bulk viscosity for large-eddy simulation of turbulent flows with shocks. *Journal of Computational Physics* 2009; **228**(19):7368–7374.
42. Gojani A, Ohtani K, Takayama K, Hosseini S. Shock hugoniot and equations of states of water, castor oil, and aqueous solutions of sodium chloride, sucrose and gelatin. *Shock Waves* 2009; :1–6.
43. Fiorina B, Lele SK. An artificial nonlinear diffusivity method for supersonic reacting flows with shocks. *Journal of Computational Physics* 2007; **222**(1):246–264.
44. Shen Y, Zha G. Generalized finite compact difference scheme for shock/complex flowfield interaction. *Journal of Computational Physics* 2011; **230**(12):4419–4436.
45. Shu CW, Osher S. Efficient implementation of essentially non-oscillatory shock-capturing schemes. *Journal of Computational Physics* 1988; **77**(2):439–471.
46. Cook AW. Enthalpy diffusion in multicomponent flows. *Physics of Fluids (1994-present)* 2009; **21**(5).
47. Lele SK. Compact finite difference schemes with spectral-like resolution. *Journal of computational physics* 1992; **103**(1):16–42.
48. Gaitonde DV, Visbal MR. Pade-plusmn;-type higher-order boundary filters for the navier-stokes equations. *AIAA journal* 2000; **38**(11):2103–2112.
49. Kawai S, Terashima H. A high-resolution scheme for compressible multicomponent flows with shock waves. *International Journal for Numerical Methods in Fluids* 2011; **66**(10):1207–1225.

50. Cocchi J, Saurel R, Loraud J. Treatment of interface problems with godunov-type schemes. *Shock Waves* 1996; **5**(6):347–357.
51. Bagabir A, Drikakis D. Mach number effects on shock-bubble interaction. *Shock Waves* 2001; **11**(3):209–218.
52. Quirk JJ, Karni S. On the dynamics of a shock–bubble interaction. *Journal of Fluid Mechanics* 1996; **318**:129–163.
53. Schmidmayer K, Petitpas F, Daniel E, Favrie N, Gavrilyuk S. A model and numerical method for compressible flows with capillary effects. *Journal of Computational Physics* 2017; **334**:468–496.
54. Garrick DP, Owkes M, Regele JD. A finite-volume hllc-based scheme for compressible interfacial flows with surface tension. *Journal of Computational Physics* 2017; **339**:46–67.
55. Igra D, Takayama K. Numerical simulation of shock wave interaction with a water column. *Shock Waves* 2001; **11**(3):219–228.
56. Meng J, Colonius T. Numerical simulations of the early stages of high-speed droplet breakup. *Shock Waves* 2015; **25**(4):399–414.